Results in Physics 16 (2020) 102811

Contents lists available at ScienceDirect

Results in Physics

journal homepage: www.elsevier.com/locate/rinp

Numerical simulation of multi-color laser generation in Tm-doped tellurite microsphere at 1.9, 1.5 and 2.3 microns

E.A. Anashkina[a,*], G. Leuchs[a,b], A.V. Andrianov[a]

[a] Institute of Applied Physics of the Russian Academy of Sciences, Nizhny Novgorod, Russia
[b] Max Planck Institute for the Science of Light, Erlangen, Germany

ARTICLE INFO

Keywords:
Microlaser
Tellurite microsphere
Microresonator
Multi-color generation
Tm-doped tellurite glass

ABSTRACT

We present the first detailed theoretical analysis of multi-color continuous wave lasing in Tm-doped tellurite spherical microresonators with whispering gallery modes pumped at a wavelength of 792 nm. The numerical model is based on solving a system of equations for intracavity field amplitudes and rate equations using the parameters of Tm-doped tellurite glass measured in the previous experiments. All fundamental whispering gallery modes in the gain bands are taken into account. We demonstrate diagrams of generation regimes depending on Q-factors and pump power, which show a possibility of single-color lasing at a wavelength of ~1.9 μm, two-color lasing at wavelengths of ~1.9&1.5 μm and at ~1.9&2.3 μm, and three-color lasing at wavelengths of ~1.9&1.5&2.3 μm. Such microlasers can play a significant role in sensing applications.

Introduction

Whispering gallery mode (WGM) microlasers operating in the near and mid-IR are demanded for many applications, in particular, for sensing [1–4]. WGM microlasers have low pump thresholds, narrow linewidths, and compact sizes. The sensors on their basis allow detecting nanoparticles, gases and biocomponents [1–4]. The radiation at wavelengths (λ) of ~1.5 μm, ~1.9 μm and ~2.3 μm corresponds to some absorption lines of several chemical compounds (for example, acetylene and ammonia at λ ~1.5 μm; CO_2 at λ ~1.9–2 μm, glucose, protein, hydrocarbons, CO, and HF at λ ~2.3 μm), so microlasers at these wavelengths can also find specific application. Such microlasers can play a significant role in trace level detection of gases required in environmental sensing, homeland security, agriculture and health care [5].

The three wavelengths mentioned above can be generated in Tm-doped active elements (a simplified energy scheme is shown in Fig. 1(a)). Tm-doped microlasers operating near 1.9–2 μm at the $^3F_4 \rightarrow {}^3H_6$ energy transition were demonstrated on the basis of silica [6–8], tellurite [9,10], and chalcogenide [11] glasses. Two-color cascade lasing at ~1.5&1.9 μm (at the sequential transitions $^3H_4 \rightarrow {}^3F_4$ and $^3F_4 \rightarrow {}^3H_6$) was also reported for Tm-doped tellurite microspheres [12,13]. Recently, Tm-Ho-co-doped tellurite microspheres were implemented for lasing at 1.47 μm [14] and at 2.1 μm [15]. Several Tm-doped glasses such as fluoride and tellurite also allow generation at 2.3 μm at the $^3H_4 \rightarrow {}^3H_5$ transition [16–18], but we have no information about microlasers at 2.3 μm on their basis. Wavelengths of ~1.5 μm and 2.3 μm cannot be generated in Tm-doped silica glass due to multiphonon relaxation that limits the lifetime of the excited state $^3H_4$, so special glasses are required for the development of Tm-doped microlasers generating from the $^3H_4$ level. Fluoride and tellurite glasses are good candidates. Current technologies make it possible to create high-quality, high-purity, low-loss tellurite glasses [19–26]. They are stronger mechanically and possess better chemical stability, have higher glass transition temperatures and lower coefficients of thermal expansion than the fluoride ones [20]. Many compositions are resistant to crystallization [19,21,22]. As the stimulated emission cross-section related to the refractive index of host glasses is expressed by $\sigma_{em} \sim (n^2 + 2)^2/n$, tellurite glasses with n ~2 are capable of providing a large stimulated emission cross-section over a broader band than fluoride glasses with n ~ 1.5. Fig. 1(b) shows the emission and absorption cross-sections for Tm-doped zinc-tellurite glass [21].

Despite the rather large number of experimental papers on Tm-doped microlasers [6–15], we have not found theoretical ones. Here, for the first time to the best of our knowledge, we give a detailed theoretical analysis of lasing in Tm-doped microspheres. We investigate a tellurite host glass for the reasons enumerated above. However, the developed numerical model can be also used for modeling Tm-doped microlasers based on other glasses using the corresponding constants (such as lifetimes of energy levels, cross-sections of stimulated

* Corresponding author.
E-mail address: elena.anashkina@ipfran.ru (E.A. Anashkina).

https://doi.org/10.1016/j.rinp.2019.102811
Received 25 June 2019; Received in revised form 12 November 2019; Accepted 12 November 2019
Available online 17 November 2019

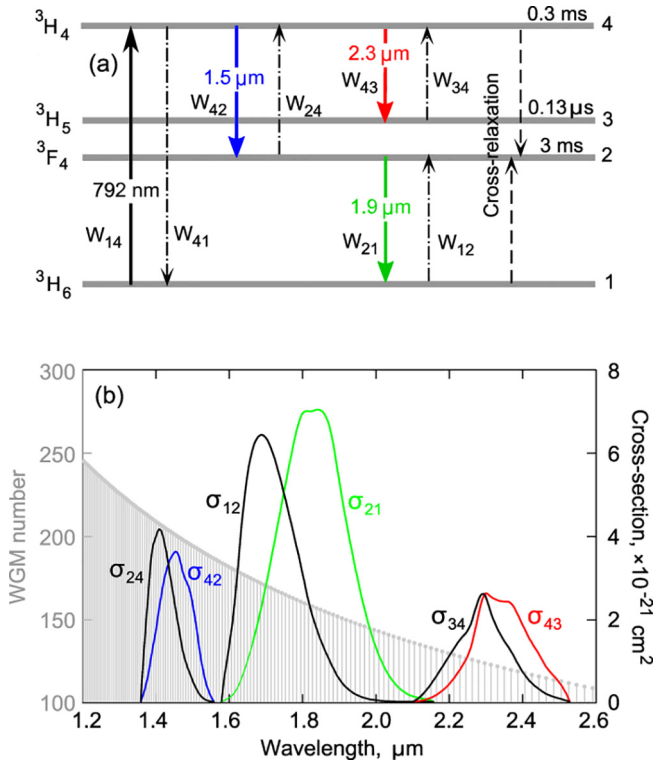

Fig. 1. (a) Simplified scheme of energy levels of Tm^{3+} in tellurite glass matrix. (b) Emission and absorption cross-sections of $^3H_4 \rightarrow {}^3F_4$, $^3F_4 \rightarrow {}^3H_6$, and $^3H_4 \rightarrow {}^3H_5$ transitions (right axis) and orders of the fundamental WGMs (grey stems, left axis).

transitions, cross-relaxation constants, etc.). Here we assume the characteristics of the considered tellurite glass to be the same as in our previous experiment [21]. We show that there are several continuous wave (CW) laser regimes in the system for different parameters. We present diagrams of generation regimes depending on Q-factors and pump power at 792 nm which demonstrate the potential of single-color lasing at ~1.9 μm, two-color lasing at ~1.9&1.5 μm and at ~1.9& 2.3 μm, and three-color lasing at ~1.9&1.5&2.3 μm.

Theoretical model

The scheme of the considered system is shown in Fig. 2. It consists of a tellurite microsphere and a tapered fiber for both, coupling the pump wave and extracting the generated laser radiation. Here and further $d = 50$ μm is the microsphere diameter and $b = 2.5$ μm is the thickness of a Tm-doped outer layer. We assume that the refractive indices of undoped and doped glasses are the same. We take a relatively small size of the microsphere to provide a sufficiently large frequency distance

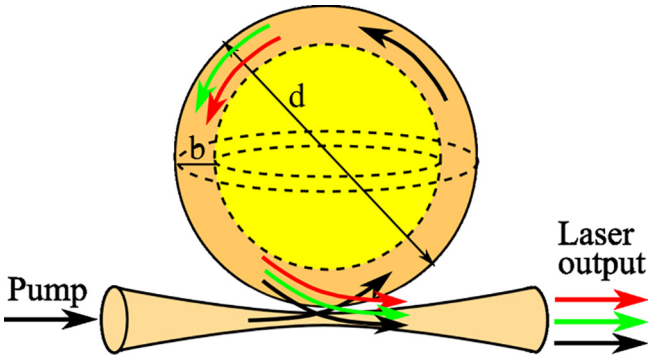

Fig. 2. Scheme of the considered system.

between neighboring WGMs for suppressing the mode competition within the single gain band.

It is known that when coupling an electromagnetic wave through a fiber taper, the HE_{11} fiber mode effectively excites the TE mode of the microsphere [27]. Therefore, here we consider the TE microsphere modes. Note that we used a similar geometry earlier aimed at forming optical frequency combs in nonlinear undoped spherical microresonators [28–30]. The problem of finding the eigenmodes of a dielectric sphere from the Helmholtz equation is well studied [4,31]. The eigenmodes are characterized by three orders (or indices) l, m, and q. The mode order l indicates the order of the spherical harmonic that describes the angular field distribution. This function is the eigenfunction of the square of the orbital momentum operator [4]. The m order is called the azimuthal mode order and can take on $2l + 1$ values from $-l$ to $+ l$. The q order characterizes the number of mode nodes inside the sphere in the radial direction. Here we consider the fundamental WGMs for which the mode order l coincides with the azimuthal order m ($l = m$) and $q = 1$ (due to the assumption that the microsphere is only doped in the outer layer, and the most amplified WGMs are the fundamental ones). In this case the eigenfrequencies ν_l can be estimated using the approximation formula [31]:

$$\nu_l = \frac{c}{\pi d\sqrt{\varepsilon}}\left[(l+1/2) + 1.85576(l+1/2)^{1/3} - \left(\frac{\varepsilon}{\varepsilon-1}\right)^{1/2}\right] \quad (1)$$

where c is the speed of light and ε is the permittivity of tellurite glass. The permittivity is a square of the refractive index defined by the Sellmeyer equation:

$$\varepsilon = A + \frac{B}{1 - C/\lambda^2} + \frac{D}{1 - E/\lambda^2} \quad (2)$$

$\lambda = c/\nu$ is wavelength, $A = 2.184$, $B = 1.617$, $C = 0.05372$ μm^2, $D = 2.476$, and $E = 225$ μm^2 (these coefficients were taken on the basis of the experimental data presented in [19]). We have also checked that the direct numerical solution of the characteristic equation (which can be found, for example in [31]), in our case gives very close values of eigenfrequencies as compared to ν_l defined by (1). The calculated values of the orders of the fundamental WGMs as a function of wavelength are shown in Fig. 1(b) (grey stems, left axis). We take into account all the WGMs in the gain band corresponding to the laser transitions $^3H_4 \rightarrow {}^3F_4$, $^3F_4 \rightarrow {}^3H_6$, and $^3H_4 \rightarrow {}^3H_5$ (4 → 2, 2 → 1, and 4 → 3, respectively, see Fig. 1(b)). The emission cross-sections σ_{42}, σ_{21}, and σ_{43} were calculated from the measured luminescence spectra of the Tm-doped tellurite glass [16] using the Füchtbauer-Ladenburg equation [32], and then the absorption cross-sections σ_{24}, σ_{12} and σ_{34} were found via the McCumber theory [33] (see Fig. 1 (b), right axis).

An important characteristic is also the effective field area S_l^{eff} of WGM with order l:

$$S_l^{eff} = V_l^{eff}/(\pi d) \quad (3)$$

here V_l^{eff} is the effective WGM volume estimated using the approximation formula [34]:

$$V_l^{eff} \approx 3.4\pi^{3/2}[\lambda/(2\pi\sqrt{\varepsilon})]^3 l^{11/6} \quad (4)$$

We found that the WGM orders closest to the maxima of emission cross-sections of the $^3H_4 \rightarrow {}^3F_4$, $^3F_4 \rightarrow {}^3H_6$, and $^3H_4 \rightarrow {}^3H_5$ transitions are $l = 201$, 157, 124, respectively (see Fig. 1(b)). The effective field areas for them are $S_{l=201}^{eff} = 3.4$ μm^2, $S_{l=157}^{eff} = 4.4$ μm^2, and $S_{l=124}^{eff} = 5.6$ μm^2. We also set the pump wavelength to be 792 nm ($l = 381$, $S_{l=381}^{eff} = 1.7$ μm^2). Further we neglected the difference between the effective field areas for different WGM orders inside a single gain band and took $S_{41}^{eff} = S_{l=381}^{eff}$, $S_{42}^{eff} = S_{l=201}^{eff}$, $S_{21}^{eff} = S_{l=157}^{eff}$, and $S_{43}^{eff} = S_{l=124}^{eff}$, where the subscripts $xy = 41$, 42, 21, and 43 now indicate the energy transitions (see Fig. 1(a)).

The laser behavior is simulated using the parameters mentioned above with allowance for the simplified four-level energy scheme

shown in Fig. 1(a). The rate equations for the population densities n_1, n_2, n_3, n_4 (normalized to the concentration of Tm^{3+} ions $N_{Tm} = 5{\cdot}10^{19}$ cm^{-3} in the doped outer layer) are given by [21,35,36]:

$$\frac{dn_1}{dt} = -(W_{14} + W_{12})n_1 + \left(W_{21} + \frac{1}{\tau_2}\right)n_2 + \left(W_{41} + \frac{\beta_{41}}{\tau_4^R}\right)n_4 - K_{CR}n_4n_1 \quad (5)$$

$$\frac{dn_2}{dt} = W_{12}n_1 - \left(W_{21} + W_{24} + \frac{1}{\tau_2}\right)n_2 + \frac{n_3}{\tau_3} + \left(W_{42} + \frac{\beta_{42}}{\tau_4^R}\right)n_4 + 2K_{CR}n_4n_1 \quad (6)$$

$$\frac{dn_3}{dt} = -\left(W_{34} + \frac{1}{\tau_3}\right)n_3 + \left(W_{43} + \frac{1}{\tau_4^{NR}} + \frac{\beta_{43}}{\tau_4^R}\right)n_4 \quad (7)$$

$$\frac{dn_4}{dt} = W_{14}n_1 + W_{24}n_2 + W_{34}n_3 - \left(W_{41} + W_{42} + W_{43} + \frac{1}{\tau_4}\right)n_4 - K_{CR}n_4n_1 \quad (8)$$

$$n_1 + n_2 + n_3 + n_4 = 1 \quad (9)$$

Of the four Eqs. (5)–(8), only three are independent. Here τ_4, ${\tau_4}^R$ and ${\tau_4}^{NR}$ are the total, radiative and non-radiative lifetimes of level 4, respectively ($\tau_4 = 0.3$ ms [16], ${\tau_4}^R = 0.4$ ms [35], ${\tau_4}^{NR} = (1/\tau_4 - 1/{\tau_4}^R)^{-1} = 1.2$ ms); τ_3 is the total (nonradiative) lifetime of level 3 ($\tau_3 = 0.13$ μs [16]); τ_2 is the total lifetime of level 2 ($\tau_2 = 3$ ms [16,35]); β_{4y} is the branching ratio from level 4 to level $y = 1, 2, 3$ ($\beta_{41} = 0.9$, $\beta_{42} = 0.07$, $\beta_{43} = 0.03$ [35]); K_{CR} is the cross-relaxation coefficient ($K_{CR} = 1000\ s^{-1}$ [35]). W_{xy} are the stimulated emission and absorption rates:

$$W_{xy} = \frac{\Gamma_{xy}}{hcS_{xy}^{eff}} \sum_l \lambda_{xy,l}\sigma_{xy,l}\,|A_{xy,l}|^2 \quad (10)$$

where h is Planck's constant. The overlap factors Γ_{xy} of WGMs with the Tm-doped layer are estimated to be $\Gamma_{41} = 0.99$, $\Gamma_{42} = 0.92$, $\Gamma_{21} = 0.9$, and $\Gamma_{43} = 0.85$.

The evolution of the time-dependent intracavity field amplitudes $A_{xy,l}$ inside the microsphere are described by the coupled differential equations [27,37,38]:

$$\frac{dA_{41,l}}{dt} = -\frac{1}{2}\left(\frac{1}{T_{41,l}^0} + \frac{1}{T_{41,l}^{ext}} - g_{41,l} - 2i\delta_{41}\right)A_{41,l} + i\sqrt{\frac{1}{T_{41,l}^{ext}T_{41,l}^{RT}}}E_{pump} \quad (11)$$

$$\frac{dA_{21,l}}{dt} = -\frac{1}{2}\left(\frac{1}{T_{21,l}^0} + \frac{1}{T_{21,l}^{ext}} - g_{21,l}\right)A_{21,l} \quad (12)$$

$$\frac{dA_{42,l}}{dt} = -\frac{1}{2}\left(\frac{1}{T_{42,l}^0} + \frac{1}{T_{42,l}^{ext}} - g_{42,l}\right)A_{42,l} \quad (13)$$

$$\frac{dA_{43,l}}{dt} = -\frac{1}{2}\left(\frac{1}{T_{43,l}^0} + \frac{1}{T_{43,l}^{ext}} - g_{43,l}\right)A_{43,l} \quad (14)$$

where δ_{41} is detuning of the pump from the exact resonance with the nearest WGM (further we take $\delta_{41} = 0$), $g_{xy,l}$ are the gains calculated as [37,38]:

$$g_{41,l} = \frac{c\Gamma_{41}N_{Tm}}{\sqrt{\varepsilon}}[\sigma_{41,l}n_4 - \sigma_{14,l}n_1] \quad (15)$$

$$g_{21,l} = \frac{c\Gamma_{21}N_{Tm}}{\sqrt{\varepsilon}}[\sigma_{21,l}n_2 - \sigma_{12,l}n_1] \quad (16)$$

$$g_{42,l} = \frac{c\Gamma_{42}N_{Tm}}{\sqrt{\varepsilon}}[\sigma_{42,l}n_4 - \sigma_{24,l}n_2] \quad (17)$$

$$g_{43,l} = \frac{c\Gamma_{43}N_{Tm}}{\sqrt{\varepsilon}}[\sigma_{43,l}n_4 - \sigma_{34,l}n_3] \quad (18)$$

$T_{41,l}^0$, $T_{21,l}^0$, $T_{42,l}^0$, and $T_{43,l}^0$ are the intrinsic lifetimes; $T_{41,l}^{ext}$, $T_{21,l}^{ext}$, $T_{42,l}^{ext}$, and $T_{43,l}^{ext}$ are the coupling lifetimes; $T_{xy,l}^{RT}$ is the round trip time (circulating time inside the microsphere $T_{xy,l}^{RT} \approx 1$ ps). We neglect the difference between the lifetimes for different WGM orders inside a single gain band. The intrinsic lifetimes are

$$T_{xy}^0 = Q\lambda_{xy}/(2\pi c) \quad (19)$$

They are related to the total intrinsic quality factor Q of the microspheres and are typically limited by the material or scattering losses. The quality factor can be approximated by [39]

$$Q^{-1} \approx Q_{mat}^{-1} + Q_{scat}^{-1} \approx \frac{\alpha\lambda}{2\pi\sqrt{\varepsilon}} + \frac{2\pi^2\sigma^2L}{\lambda^2 d} \quad (20)$$

where α is the bulk material attenuation, σ and L are the root mean square (RMS) size and correlation length of the surface inhomogeneities. If material losses are dominant, then

$$T_{41}^0 = \frac{\sqrt{\varepsilon}}{\alpha c} \quad (21)$$

So, in this case the intrinsic lifetimes do not depend on wavelength. If scattering losses are significant, the intrinsic lifetimes may be shorter for shorter wavelengths.

The coupling coefficients and lifetimes may be calculated using the corresponding theory [27,40]. We estimate that for fiber tapers with the waist of about 1–2 μm and the sub-micron gap between the microsphere and the taper, the coupling coefficient at the pump wavelength may be of the order of 10^{-4}, but at the laser wavelengths they may be of the order of 10^{-7}–10^{-5} (depending on the fiber waist, the tapered angle and the gap). We take the coupling lifetimes $T_{41}^{ext} = 10^{-8}$ s and $T_{42}^{ext} = T_{21}^{ext} = T_{43}^{ext} = 10^{-6}$ s corresponding to the coupling coefficient of 10^{-4} at a pump wavelength and 10^{-6} at laser wavelengths. Even if the coupling lifetimes for different gain bands are different, this fact does not affect the calculation of the intracavity fields and powers $P_{xy,l}$, since these coupling lifetimes are much longer than the intrinsic lifetimes. However, this fact affects the output laser powers $P_{xy,l}^{out}$ [27,40]:

$$P_{xy,l}^{out} = \left|\sqrt{\frac{T_{xy}^{RT}}{T_{xy}^{ext}}}A_{xy,l}\right|^2 = \frac{T_{xy}^{RT}}{T_{xy}^{ext}}P_{xy,l} \quad (22)$$

here $xy = 42, 21, 43$.

Simulation methods

In fact, system (5)–(8), (11)–(14) taking into account expressions (9), (10), and (15)–(18) contains more than 100 first-order differential nonlinear equations, since many WGMs are within the region of non-zero emission cross-sections and any of these modes can lase, in principle, so the system may have a rich variety of generation regimes. The system dynamics can be studied by direct numerical integration of a set of differential equations starting from noise initial conditions. After a long enough simulation time (after decay of relaxation oscillations), the system tends to the equilibrium state, thus steady-state values of intensities and populations can be obtained in numerical modeling. However, this method is very time consuming, if used in many realizations for different pump powers and Q-factors. For determining CW generation regimes, a steady-state solution of the system can be found by solving a set of nonlinear algebraic equations obtained by letting d/dt = 0. However, the system of the order of 100 nonlinearly coupled algebraic equations cannot be readily solved. Further we propose a semi-analytical method allowing us to solve this system and find a stable solution. Our original approach which allows solving only a single nonlinear algebraic equation (rather than a system) with a power not higher than 4 relative to one of n_i and further express the other n_i and electric field magnitudes A_i in terms of this value. A single nonlinear algebraic equation is solved many times using exhaustive search for each WGM for single-color generation and all possible combinations

of WGMs from different active bands for two-color and three-color generation assuming that no more than one WGM can be generated in each gain band. After that only physically meaningful stable solutions ($P_{xy,l} > 0$ and $0 < n_{1,2,3,4} < 1$) are chosen. Stability of the solutions is discussed at the end of this section. For comparison, we also made an independent numerical integration of the differential equations by the Runge-Kutta method. The initial conditions are low-amplitude noise fields for every WGM in all gain bands or square roots of laser powers found by the first method plus noise for all WGMs (to be discussed below). The direct Runge-Kutta simulation is also used to confirm the assumption that in each gain band no more than one WGM can be generated. Comparison of the results obtained by the two methods allows confirming their reliability.

In principle, the following cases of CW lasing (or its absence) are possible in our model:

I. No lasing at 4 → 2, 2 → 1 and 4 → 3 transitions.
II. Lasing only at 4 → 2 transition near 1.5 μm.
III. Lasing only at 2 → 1 transition near 1.9 μm.
IV. Lasing only at 4 → 3 transition near 2.3 μm.
V. Two-color lasing at 4 → 2 and 2 → 1 transitions simultaneously.
VI. Two-color lasing at 4 → 2 and 4 → 3 transitions simultaneously.
VII. Two-color lasing at 2 → 1 and 4 → 3 transitions simultaneously.
VIII. Three-color lasing at 4 → 2, 2 → 1 and 4 → 3 transitions simultaneously.

For case I, $A_{42,l} = A_{21,l} = A_{43,l} = 0$, therefore Eqs. (5)–(7), (11) reduce to:

$$-W_{14}n_1 + \frac{n_2}{\tau_2} + \left(W_{41} + \frac{\beta_{41}}{\tau_4^R}\right)n_4 - K_{CR}n_4n_1 = 0 \tag{23}$$

$$-\frac{n_2}{\tau_2} + \frac{n_3}{\tau_3} + \frac{\beta_{42}n_4}{\tau_4^R} + 2K_{CR}n_4n_1 = 0 \tag{24}$$

$$-\frac{n_3}{\tau_3} + \left(\frac{1}{\tau_4^{NR}} + \frac{\beta_{43}}{\tau_4^R}\right)n_4 = 0 \tag{25}$$

$$\left(\frac{1}{T_{41,l}^0} + \frac{1}{T_{41,l}^{ext}} - g_{41,l}\right)^2 P_{41} = \frac{4P_{pump}}{T_{41,l}^{ext}T_{41,l}^{RT}} \tag{26}$$

and we solve Eqs. (9), (23)-(26). From this system, the polynomial equation for n_4 is obtained and, after finding the roots, all other variables are expressed through them.

For case II, $P_{42,l} \neq 0$, so from Eq. (13) follows

$$\left(\frac{1}{T_{42,l}^0} + \frac{1}{T_{42,l}^{ext}} - g_{42,l}\right) = 0 \tag{27}$$

We solve Eq. (27) together with Eqs. (26), (9) and (5)–(7) for each l from the active band. The polynomial equation for n_4 is obtained like in the previous case, and further all other variables are expressed through the roots of this equation.

Cases III and IV are analyzed analogously to case II.

For case V, $P_{42,l^*} \neq 0$ and $P_{21,l^{**}} \neq 0$, so the expressions in parentheses in the right-hand sides of Eqs. (12)–(13) must be zeros. By using these expressions together with Eqs. (7) and (9), we obtain a linear system of equations for populations (the superscript "V" means case V):

$$\begin{pmatrix} -\frac{c\Gamma_{21}N_{Tm}\sigma_{12,l^{**}}}{n_{eff}} & \frac{c\Gamma_{21}N_{Tm}\sigma_{21,l^{**}}}{n_{eff}} & 0 & 0 \\ 0 & -\frac{c\Gamma_{42}N_{Tm}\sigma_{24,l^*}}{n_{eff}} & 0 & \frac{c\Gamma_{42}N_{Tm}\sigma_{42,l^*}}{n_{eff}} \\ 0 & 0 & -\frac{1}{\tau_{32}} & \frac{1}{\tau_{43}} \\ 1 & 1 & 1 & 1 \end{pmatrix} \begin{pmatrix} n_1^V \\ n_2^V \\ n_3^V \\ n_4^V \end{pmatrix} = \begin{pmatrix} \frac{1}{T_{21,l}^0} + \frac{1}{T_{21,l}^{ext}} \\ \frac{1}{T_{42,l}^0} + \frac{1}{T_{42,l}^{ext}} \\ 0 \\ 1 \end{pmatrix} \tag{28}$$

which can be solved by Cramer's rule:

$$n_i^V = \frac{\det B_i^V}{\det B^V}, \quad i = 1,\ 2,\ 3,\ 4 \tag{29}$$

where B^V is the 4x4 matrix in the left-hand side of expression (28), B_i^V is the matrix formed by replacing the i-th column of B^V by the column vector from the right-hand side of (28). Note that the populations do not depend on pump power in this case. Next, powers P_{41}, $P_{21,l^{**}}$, P_{42,l^*} are expressed from (26), (5), (6), successively.

For case VI, $P_{42,l^*} \neq 0$ and $P_{43,l^{**}} \neq 0$, so the expressions in parentheses in the right-hand sides of Eqs. (13)–(14) must be zeros. With the use of rate equations, it is possible to write a polynomial equation for n_1 and express other variables successively through the roots of this equation.

Case VII is analyzed analogously to case VI.

For Case VIII, CW lasing occurs at three transitions 4 → 2, 2 → 1, and 4 → 3 simultaneously. In this regime the expressions in parentheses in the right-hand sides of Eqs. (12)-(14) must be equal to zero, and the populations can be found from these conditions with allowance for Eq. (9) from the following linear system of equations

$$\begin{pmatrix} -\frac{c\Gamma_{21}N_{Tm}\sigma_{12,l}}{n_{eff}} & \frac{c\Gamma_{21}N_{Tm}\sigma_{21,l}}{n_{eff}} & 0 & 0 \\ 0 & -\frac{c\Gamma_{42}N_{Tm}\sigma_{24,l}}{n_{eff}} & 0 & \frac{c\Gamma_{42}N_{Tm}\sigma_{42,l}}{n_{eff}} \\ 0 & 0 & -\frac{c\Gamma_{43}N_{Tm}\sigma_{34,l}}{n_{eff}} & \frac{c\Gamma_{43}N_{Tm}\sigma_{43,l}}{n_{eff}} \\ 1 & 1 & 1 & 1 \end{pmatrix} \begin{pmatrix} n_1^{VIII} \\ n_2^{VIII} \\ n_3^{VIII} \\ n_4^{VIII} \end{pmatrix} = \begin{pmatrix} \frac{1}{T_{21,l}^0} + \frac{1}{T_{21,l}^{ext}} \\ \frac{1}{T_{42,l}^0} + \frac{1}{T_{42,l}^{ext}} \\ \frac{1}{T_{43,l}^0} + \frac{1}{T_{43,l}^{ext}} \\ 1 \end{pmatrix} \tag{30}$$

by Cramer's rule:

$$n_i^{VIII} = \frac{\det B_i^{VIII}}{\det B^{VIII}}, \quad i = 1,\ 2,\ 3,\ 4 \tag{31}$$

where B^{VIII} is the 4x4 matrix in the left-hand side of (30), B_i^{VIII} is the matrix formed by replacing the i-th column of B^{VIII} by the column vector from the right-hand side of (30), the superscript 'VIII' means case VIII.

It is interesting to note that the populations do not depend on pump power for three-color CW generation. Moreover, the power of the wave at 2.3 μm is also independent of the pump power and can be found taking into account the populations obtained by formula (31) from Eq. (7):

$$P_{43,l} = \frac{hcS_{eff}\left(\frac{n_3^{VIII}}{\tau_3} - \frac{n_4^{VIII}}{\tau_4^{NR}} - \frac{\beta_{43}n_4^{VIII}}{\tau_4^R}\right)}{\Gamma_{43}\lambda_{43}(\sigma_{43,l}n_4^{VIII} - \sigma_{34,l}n_3^{VIII})} \tag{32}$$

Exhaustive search among cases I-VIII for all possible WGMs (no more than one WGM in each active band) is performed for each set of parameters and the conditions $P_{xy,l} > 0$ and $0 < n_{1,2,3,4} < 1$ are verified. Among the remaining solutions we choose only the stable ones as follows. If a WGM with order l^* is generated in the system only, then for all other WGMs with orders $l \neq l^*$ the zero solution ($A_{xy,l} = 0$) must be stable, i.e. the increment in Eqs. (12)–(14) must be negative:

$$-\frac{1}{2}\left(\frac{1}{T_{l\neq l*}^0} + \frac{1}{T_{l\neq l*}^{ext}} - g_{l\neq l*}\right) < 0 \tag{33}$$

Analogously, for the case of generating two (three) waves with WGM orders l^*, l^{**} (l^*, l^{**}, l^{***}) at different laser transitions, the increment for all other WGMs with orders $l \neq l^* \neq l^{**}$ ($l \neq l^* \neq l^{**} \neq l^{***}$) must be negative. If there is no lasing, then all the increments must be negative. After rejecting solutions that do not satisfy these

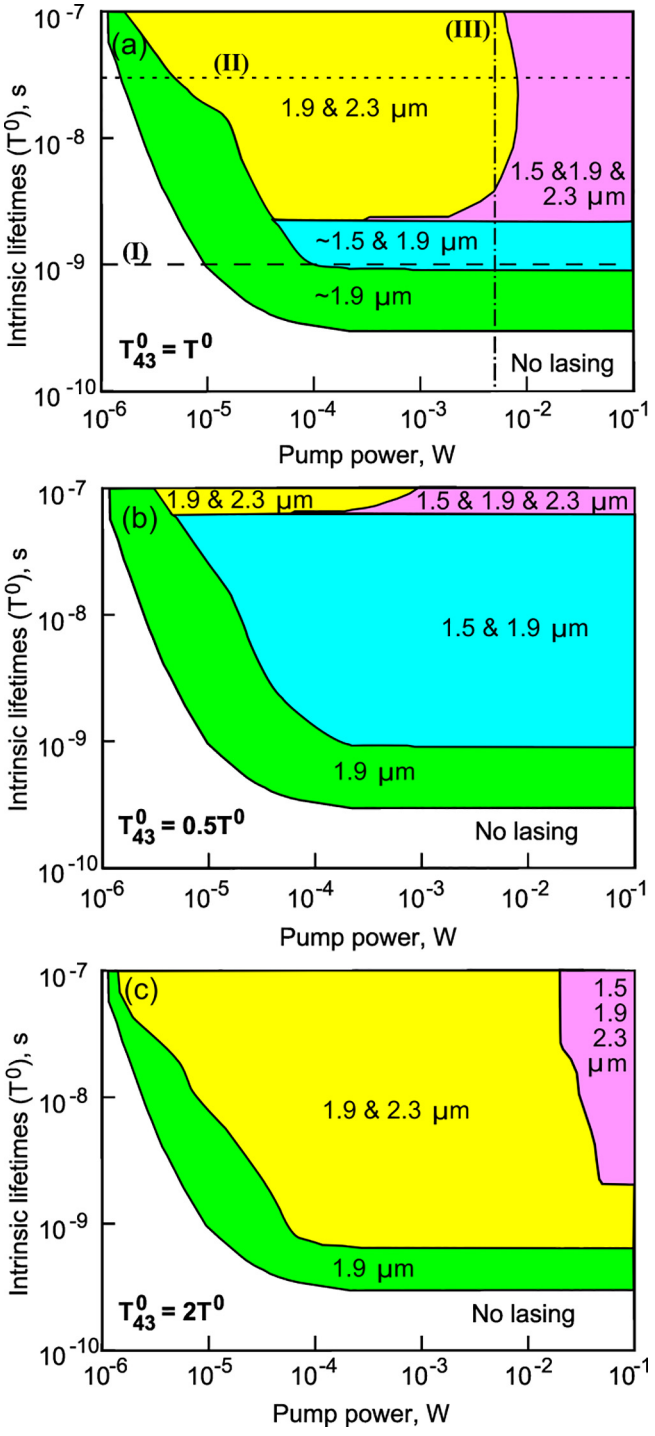

Fig. 3. Diagrams of generation regimes for (a) $T^0_{41} = T^0_{21} = T^0_{42} = T^0_{43} = T^O$, (b) $T^0_{41} = T^0_{21} = T^0_{42} = T^O$ and $T^0_{43} = 0.5{\cdot}T^O$, (c) $T^0_{41} = T^0_{21} = T^0_{42} = T^O$ and $T^0_{43} = 2{\cdot}T^O$.

conditions, we run a numerical algorithm based on the Runge-Kutta method for a full system of about 100 Eqs. (5)–(8), (11)–(14) using each of the remaining solutions as the initial conditions (adding noise in all WGMs). We have found that for each set of parameters there is exactly one stable solution.

After investigating the system behavior for different parameters we have run the algorithm based on the Runge-Kutta method with noise initial conditions for some set of parameters and have obtained a very good agreement with the solutions obtained by the algebraic method for the steady states. Note that the Runge-Kutta algorithm starting from noise is executed much longer than the algorithm based on solving a system of algebraic equations.

Results and discussion

We have analyzed the possibility of lasing in WGM microresonators with intrinsic quality factors from 10^5 to 10^8 at different pump powers. If the Q-factor of the microsphere is determined by the material losses, and the values of these losses do not depend on the wavelength, then the intrinsic lifetimes are the same at all wavelengths ($T^0_{41} = T^0_{21} = T^0_{42} = T^0_{43} = T^O$). Fig. 3(a) demonstrates a diagram of the expected generation regimes as a function of the pump power and T^O. This diagram is plotted as follows. We discretize the considered intervals for the pump power (from 0 up to 100 mW) and the intrinsic lifetime T^O (from 10^{-10} to 10^{-7} s), and for all possible pairs of values (P_{pump}, T^O) we check the possibility of implementing each of the cases I-VIII listed in the section Simulation methods (including exhaustive search for all WGMs in the gain bands). The value of the intracavity laser power of 10^{-10} W is selected as a criterion for the generation threshold. We have found that for all pairs (P_{pump}, T^O), strictly one of the cases I-VIII is realized (there is no bistability). If $T^O < 3{\cdot}10^{-10}$ s, which corresponds to the quality factor $Q < 3{\cdot}10^5$, no generation is observed. The laser threshold is reached first at the $2 \rightarrow 1$ transition for $Q > 3{\cdot}10^5$. For $T^O > 9{\cdot}10^{-10}$ s with pump power increasing after the first threshold for a wave at ~1.9 μm, the second threshold for laser generation is reached at the $4 \rightarrow 2$ or $4 \rightarrow 3$ transition, so two-color generation is observed at 1.9&1.5 μm or 1.9&2.3 μm, respectively. For $0.9{\cdot}10^{-9} < T^0 < 2{\cdot}10^{-9}$ s generation is expected at 1.9&1.5 μm. With a further power increase for these Q-factors, there is no qualitative change in the system behavior. Note that this regime was observed experimentally in [12,13]. For $T^0 > 2{\cdot}10^{-9}$ s with pump power increasing after reaching the first threshold of 1.9 μm, the second threshold at 2.3 μm can be achieved. For a further pump increase, the third threshold for a 1.5 μm wave is reached, and three-color lasing is observed in the system. The two-color generation at 1.9&2.3 μm has not been demonstrated in microlasers experimentally, but was obtained in a Tm-doped tellurite optical fiber [21].

Let's assume that losses at 2.3 μm become higher than at other wavelengths (which may be, for example, due to absorption by hydroxyl groups). This leads to a decrease of the Q-factor at 2.3 μm and of T^0_{43}. In this case, the areas of lasing at 1.9&2.3 μm and at 1.9&2.3& 1.5 μm shift upwards in the diagram of the generation regimes. So generation at 2.3 μm is possible only for larger T^0_{43} than in the case of equality of all intrinsic lifetimes $T^0_{xy} = T^O$. A diagram for $T^0_{43} = T^O/2$, qualitatively similar to the diagram in Fig. 3(a), is shown in Fig. 3(b). At the same time, lasing at 2.3 μm in a cascade scheme is possible only for $T^0_{43} > 6{\cdot}10^{-8}$ s ($Q > 6{\cdot}10^7$@2.3 μm), while for $T^0_{43} = T^O$, lasing at 2.3 μm is possible for $T^0_{43} > 2{\cdot}10^{-9}$ ($Q > 2{\cdot}10^6$@2.3 μm). That is, the deterioration of conditions for lasing at 2.3 μm also leads to improved conditions for lasing at 1.5 μm, since the generation occurs from the same level $^3H_4$.

Now let's assume that the intrinsic lifetime T^0_{43} for the wave at 2.3 μm becomes longer than the intrinsic lifetimes at other wavelengths. This can occur, for example, if scattering losses make a noticeable contribution to the Q-factor (see formula (20)). Since the conditions for generation at 2.3 μm are better and at the same time the conditions for generation at 1.5 μm are worse, the areas of lasing at 1.9 &2.3 μm and at 1.9&2.3&1.5 μm shift down. On reaching $T^0_{43} \sim 1.2{\cdot}T^O$, the diagram of the generation regimes changes qualitatively: there is no two-color lasing at 1.9&1.5 μm at any values of T^O and pump power. Fig. 3(c) shows the diagram of the generation regimes for $T^0_{43} = 2\ T^O$.

Next, we consider how the laser power depends on the pump power at fixed values of T^O. When $T^O = 1{\cdot}10^{-9}$ s, which corresponds to the horizontal dashed line (I) in Fig. 3(a), lasing at 1.9 μm is observed first, and then the second threshold at 1.5 μm is reached (see Fig. 4(a)). Notice the low values of the first and second thresholds: about 10 μW and 100 μW, respectively. The inset shows the dependence of the laser

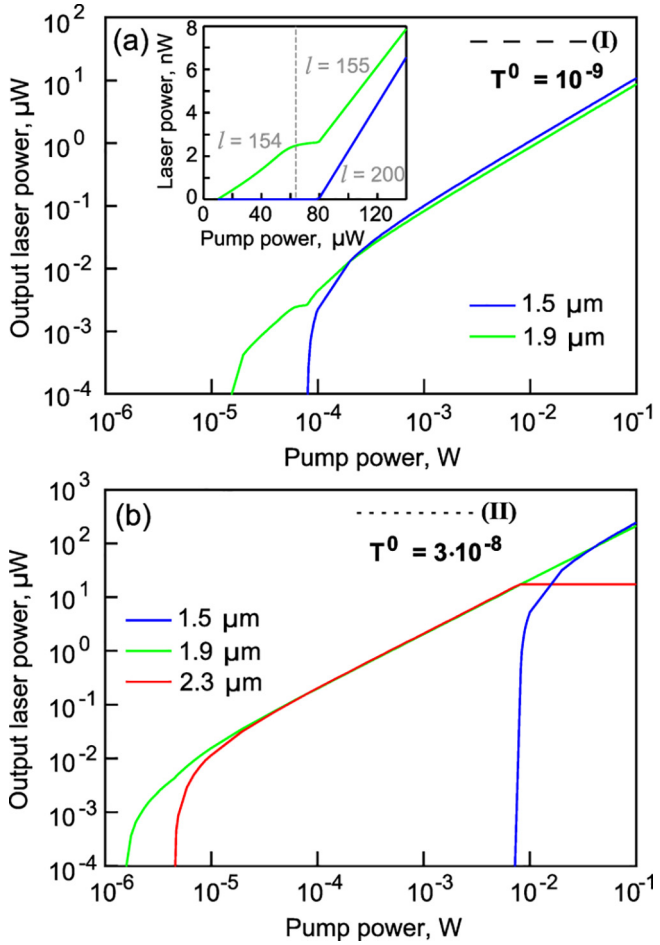

Fig. 4. Laser power *versus* pump power at fixed T^0 values: (a) $T^0 = 1{\cdot}10^{-9}$ s corresponding to the horizontal dashed line (I) in Fig. 3; (b) $T^0 = 3{\cdot}10^{-8}$ s corresponding to the horizontal dotted line (II) in Fig. 3.

powers on the pump power on a linear scale near the first and second thresholds. We note interesting features. At pump powers in the range of ~10–60 μW, a practically linear dependence is observed, only WGM $l = 154$ is generated. With a pump power of ~60–80 μW, WGM $l = 155$ is generated, therefore, a change in the slope efficiency is associated with jumping between the WGMs. The vertical dashed line corresponds to this jump (in the inset in Fig. 4(a)). Starting with a pump power of 80 μW, two waves are generated in the system ($l = 155$ and $l = 200$), the slope efficiency of the wave at 1.9 μm increases (compared to the slope efficiency in the 60–80 μW range), which fully agrees with the experimental results [12,13] and the theoretical explanation via effective levels depopulation for two-color cascade generation [21].

Let's consider $T^0 = 3{\cdot}10^{-8}$ s: the horizontal dotted line (II) in Fig. 3(a) (corresponding to material losses of 0.95 dB/m achieved for real tellurite glass samples [21]). One can see in Fig. 4(b) that the first threshold is for the wave at 1.9 μm, the second threshold is for the wave at 2.3 μm, and the third one is for the wave at 1.5 μm (1.5 μW, 4.5 μW, and 8.2 mW, respectively). The intracavity powers at 1.9 and 2.3 μm are almost the same for two-color generation. When the threshold is reached at 1.5 μm, the power of the wave at 2.3 μm stabilizes and stops changing with increasing pump power, while the powers at 1.5 and 1.9 μm continue to grow almost linearly. The stabilization of a laser power at ~2.3 μm for a certain WGM for the three-color generation is justified analytically (see expressions (30)–(32)). This is a consequence of nonradiative depopulation of level 3. There is no kink for the wave at 1.9 μm near the third threshold (because of the earlier cascade lasing at 1.9&2.3 μm).

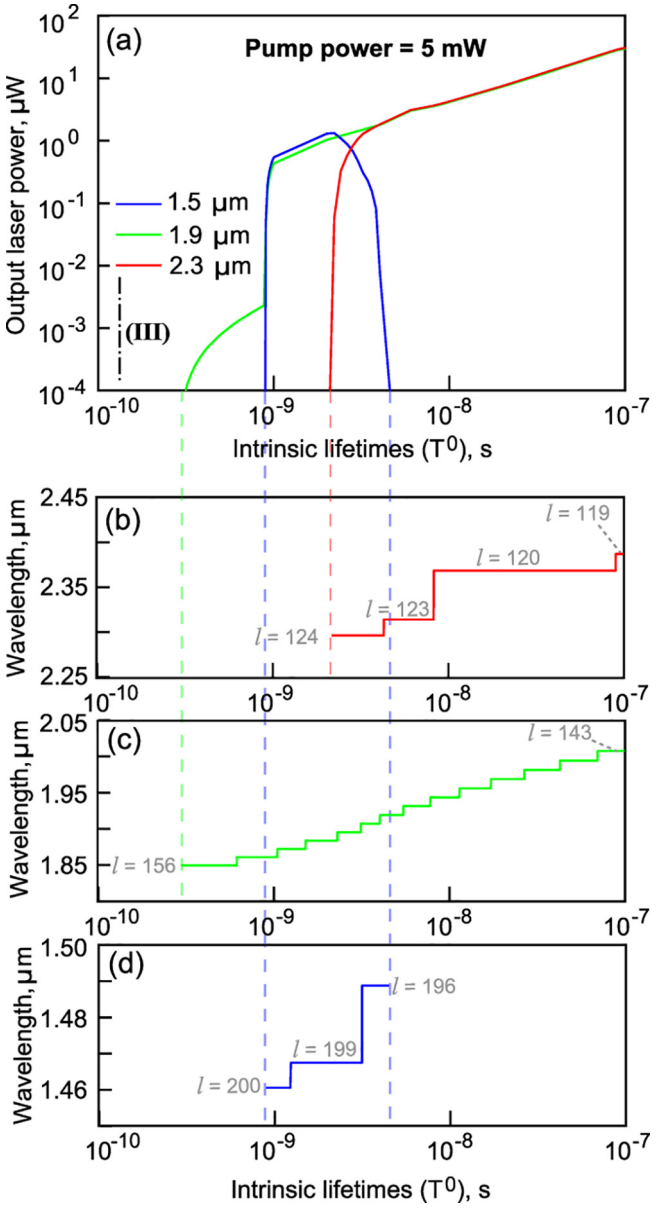

Fig. 5. (a) Laser power as a function of T^0 for constant pump power of 5 mW, which corresponds to the vertical dash-dotted line (III) in Fig. 3. Laser wavelength as a function of T^0 for $^3H_4 \rightarrow {}^3H_5$ (b), $^3F_4 \rightarrow {}^3H_6$ (c), $^3H_4 \rightarrow {}^3F_4$ (d) transitions for pump power of 5 mW.

Finally, let's consider how the laser powers vary with T^0 at a constant reasonable pump power of 5 mW, which corresponds to the vertical dash-dotted line (III) in Fig. 3(a). The corresponding curves are plotted in Fig. 5(a). First, the generation starts near 1.9 μm, with an increase in T^0 two-color lasing at 1.5&1.9 μm occurs. With a further T^0 increase, three-color generation is observed: the conditions for the wave near 2.3 μm are improved, and at the same time the conditions for the wave near 1.5 μm become worse. When $T^0 \sim 4{\cdot}10^{-9}$ s is reached, the wave at 1.5 μm ceases to be generated in the system, and only two-color generation at 1.9&2.3 μm remains. Note that this fact is due to different mechanisms of depopulation of levels 3 and 2: nonradiative and radiative, respectively. An interesting feature is a decreasing order l of the WGM generated inside each laser band with increasing T^0, which corresponds to a shift of the generated wave to a longer wavelength region with increasing Q-factor. The curves of the generated wavelengths as a function of T^0 at the pump power of 5 mW are plotted in Fig. 5(b–d) for the $4 \rightarrow 2$, $2 \rightarrow 1$, $4 \rightarrow 3$ transitions, respectively. For a wave generated

at the 2 → 1 transition, each step on the graph corresponds to a change in the WGM order by 1.

Note that single-color generation at ~1.5 μm or at ~2.3 μm and two-color generation at 2.3&1.5 μm do not arise in the system. For observing the first generation threshold at 1.5 μm or at 2.3 μm, the Q-factor at the corresponding wavelength must be significantly larger than the Q-factor at 1.9 μm, which is very difficult to implement.

Conclusion

We performed a detailed theoretical analysis of CW lasing in Tm-doped tellurite spherical WGM microresonators pumped at 792 nm. As far as we know, this is the first work devoted to numerical simulation of Tm-doped microlasers. We took for modeling the parameters of Tm-doped tellurite glass measured in earlier experiments. All fundamental WGMs in the gain bands corresponding to the energy transitions $^3H_4 \rightarrow {}^3F_4$, $^3F_4 \rightarrow {}^3H_6$, and $^3H_4 \rightarrow {}^3H_5$ at ~1.9 μm, ~1.5 μm, and ~2.3 μm, respectively, were taken into account. We chose a relatively small size (50 μm) of the microsphere to provide a sufficiently large frequency distance between neighboring WGMs for suppressing mode competition within a single gain band.

We presented diagrams of the generation regimes determined by Q-factors and pump power which demonstrated the possibility of single-color lasing at ~1.9 μm, two-color lasing at ~1.9&1.5 μm and at ~1.9& 2.3 μm, and three-color lasing at ~1.9&1.5&2.3 μm. For the Q-factor lower than $\sim 3 \cdot 10^5$, no generation was observed (for a microsphere diameter of 50 μm, Tm^{3+} concentration of $5 \cdot 10^{19}$ cm^{-3} in the outer layer with thickness 2.5 μm). The first laser threshold was reached for the wave at ~1.9 μm for $Q > 3 \cdot 10^5$. For a high enough Q-factor, the second threshold was observed at ~1.5 μm or at ~2.3 μm. If for the specific Q-factor two-color generation arose at ~1.9&1.5 μm, the further pump power increase did not lead to qualitative changes in the system behavior; there was no generation at 2.3 μm. Our result agrees with the experimental data obtained by different research groups. If at a specific Q-factor, two-color generation arose at ~1.9&2.3 μm, the further pump power increase led to the third threshold at ~1.5 μm; three-color generation occurred at ~1.9&1.5&2.3 μm.

CRediT authorship contribution statement

E.A. Anashkina: Conceptualization, Methodology, Validation, Investigation, Software, Formal analysis, Writing - original draft, Visualization, Funding acquisition. **G. Leuchs:** Writing - review & editing, Funding acquisition. **A.V. Andrianov:** Methodology, Writing - review & editing, Funding acquisition.

Declaration of Competing Interest

The authors declare that they have no known competing financial interests or personal relationships that could have appeared to influence the work reported in this paper.

Acknowledgements

The calculation of the parameters of tellurite microspheres (WGMs, effective WGM volumes, effective WGM field areas, and Q-factors) was supported by the Russian Science Foundation (Grant No. 18-72-00176).

The laser simulation was supported by the Mega-grant of the Ministry of Education and Science of the Russian Federation (Contract No. 14.W03.31.0032).

References

[1] Reynolds T, Riesen N, Meldrum A, Fan X, Hall JMM, Monro TM, et al. Fluorescent and lasing whispering gallery mode microresonators for sensing applications. Laser Photonics Rev 2017;11:1600265. https://doi.org/10.1002/lpor.201600265.

[2] He L, Özdemir ŞK, Yang L. Whispering gallery microcavity lasers. Laser Photonics Rev 2013;7:60–82. https://doi.org/10.1002/lpor.201100032.

[3] Foreman MR, Swaim JD, Vollmer F. Whispering gallery mode sensors. Adv Opt Photonics 2015;7:168–240. https://doi.org/10.1364/AOP.7.000168.

[4] Righini GC, Dumeige Y, Feron P, Ferrari M, Nunzi Conti G, Ristic D, et al. Whispering gallery mode microreson ators: fundamentals and applications. Rivista del nuovo cimento 2011. https://doi.org/10.1393/ncr/i2011-10067-2.

[5] Hodgkinson J, Tatam RP. Optical gas sensing: a review. Meas Sci Technol 2012;24:012004https://doi.org/10.1088/0957-0233/24/1/012004.

[6] Li A, Zhang J, Zhang M, Li W, Wang S, Lewis E, et al. Effect of Tm^{3+} concentration on the emission wavelength shift in Tm^{3+}-doped silica microsphere lasers. Opt Lett 2018;43:4325–8. https://doi.org/10.1364/OL.43.004325.

[7] Pal A, Chen SY, Sen R, Sun T, Grattan KTV. A high-Q low threshold thulium-doped silica microsphere laser in the 2 μm wavelength region designed for gas sensing applications. Laser Phys Lett 2013;10:085101https://doi.org/10.1088/1612-2011/10/8/085101.

[8] Fan H, Jiang X, Ding Y, Xiao M. Demonstration of ultralow-threshold 2 micrometer microlasers on chip. Sci China Phys Mech 2015;58:114204https://doi.org/10.1007/s11433-015-5669-4.

[9] Wu J, Jiang S, Qua T, Kuwata-Gonokami M, Peyghambarian N. 2 μm lasing from highly thulium doped tellurite glass microsphere. Appl Phys Lett 2005;87:211118https://doi.org/10.1063/1.2132532.

[10] Vanier F, Côté F, El Amraoui M, Messaddeq Y, Peter YA, Rochette M. Low-threshold lasing at 1975 nm in thulium-doped tellurite glass microspheres. Opt Lett 2015;40:5227–30. https://doi.org/10.1364/OL.40.005227.

[11] Yang K, Dai S, Wu Y, Nie Q. Fabrication and characterization of Ge–Ga–Sb–S glass microsphere lasers operating at 1.9 μm. 117701 Chinese Phys B 2018;27. https://doi.org/10.1088/1674-1056/27/11/117701.

[12] Sasagawa K, Yonezawa ZO, Iwai R, Ohta J, Nunoshita M. S-band Tm^{3+}-doped tellurite glass microsphere laser via a cascade process. Appl Phys Lett 2004;85:4325–7. https://doi.org/10.1063/1.1810628.

[13] Wu J, Jiang S, Peyghambarian N. 1.5-μm-band thulium-doped microsphere laser originating from self-terminating transition. Opt Express 2005;13:10129–33. https://doi.org/10.1364/OPEX.13.010129.

[14] Li A, Li W, Zhang M, Zhang Y, Wang S, Yang A, et al. Tm^{3+}-Ho^{3+} codoped tellurite glass microsphere laser in the 1.47 μm wavelength region. Opt Lett 2019;44:511–3. https://doi.org/10.1364/OL.44.000511.

[15] Yang Z, Wu Y, Yang K, Xu P, Zhang W, Dai S, et al. Fabrication and characterization of Tm^{3+}-Ho^{3+} co-doped tellurite glass microsphere lasers operating at~2.1 μm. Opt Mater 2017;72:524–8. https://doi.org/10.1016/j.optmat.2017.06.057.

[16] Vanier F, Côté F, El Amraoui M, Messaddeq Y, Peter YA, Rochette M. Low-threshold lasing at 1975 nm in thulium-doped tellurite glass microspheres. Opt Lett 2015;40:5227–30. https://doi.org/10.1364/OL.40.005227.

[17] Smart RG, Carter JN, Tropper AC, Hanna DC. Continuous-wave oscillation of Tm^{3+}-doped fluorozirconate fiber lasers at around 1.47 μm, 1.9 μm and 2.3 μm when pumped at 790 nm. Opt Commun 1991;82:563–70. https://doi.org/10.1016/0030-4018(91)90381-M.

[18] McAleavey FJ, O'Gorman J, Donegan JF, Hegarty J, Maze G. Extremely high sensitivity gas detection at 2.3 μm using a grazing incidence Tm3+ fibre laser cavity. Sens Actuat A Phys 2001;87:107–12. https://doi.org/10.1016/S0924-4247(00)00477-5.

[19] El-Mallawany RA. Tellurite glasses handbook: physical properties and data CRC Press; 2016. https://doi.org/10.1201/b11295.

[20] Tao G, Ebendorff-Heidepriem H, Stolyarov AM, Danto S, Badding JV, Fink Y, et al. Infrared fibers. Adv Opt Photon 2015;7:379–458. https://doi.org/10.1364/AOP.7.000379.

[21] Muravyev SV, Anashkina EA, Andrianov AV, Dorofeev VV, Motorin SE, Koptev MY, et al. Dual-band Tm^{3+}-doped tellurite fiber amplifier and laser at 1.9 μm and 2.3 μm. 16164 Sci Rep 2018;8. https://doi.org/10.1038/s41598-018-34546-w.

[22] Anashkina EA, Dorofeev VV, Koltashev VV, Kim AV. Development of Er^{3+}-doped high-purity tellurite glass fibers for gain-switched laser operation at 2.7 μm. Opt Mater Express 7 2017;4337–4351. https://doi.org/10.1364/OME.7.004337.

[23] Anashkina EA, Dorofeev VV, Muravyev SV, Motorin SE, Andrianov AV, Sorokin AA, et al. Possibilities of laser amplification and measurement of the field structure of ultrashort pulses in the range of 2.7 –3 μm in tellurite glass fibres doped with erbium ions. Quantum Electr 2018;48:1118–27. https://doi.org/10.1070/QEL16845.

[24] Anashkina EA, Andrianov AV, Dorofeev VV, Muravyev SV, Koptev MY, Sorokin AA, Motorin SE, Koltashev VV, Galagan BI, Denker BI. Two-color pump schemes for Er-doped tellurite fiber lasers and amplifiers at 2.7–2.8 μm. Laser Phys Lett 2019;16. https://doi.org/10.1088/1612-202X/aaf79a.

[25] Anashkina EA, et al. Reconstruction of optical pulse intensity and phase based on SPM spectra measurements in microstructured tellurite fiber in telecommunication range. J Light Technol 2019;37:4375–81. https://doi.org/10.1109/JLT.2019.2924352.

[26] Anashkina EA, Andrianov AV, Dorofeev VV, Kim AV, Koltashev VV, Leuchs G, et al. Development of infrared fiber lasers at 1555 nm and at 2800 nm based on Er-doped zinc-tellurite glass fiber. J Non-Cryst Solids 2019;525:119667https://doi.org/10.1016/j.jnoncrysol.2019.119667.

[27] Gorodetsky ML, Ilchenko VS. Optical microsphere resonators: optimal coupling to high-Q whispering-gallery modes. J Opt Soc Am B 1999;16:147–54. https://doi.org/10.1364/JOSAB.16.000147.

[28] Anashkina EA, Sorokin AA, Marisova MP, Andrianov AV. Development and numerical simulation of spherical microresonators based on SiO2 – GeO2 germano-silicate glasses for generation of optical frequency combs. Quantum Electron 2019;49:371–6. https://doi.org/10.1070/QEL16963.

[29] Anashkina EA, Marisova MP, Sorokin AA, Andrianov AV. Numerical simulation of

mid-infrared optical frequency comb generation in chalcogenide As_2S_3 microbubble resonators. Photonics 2019;6. https://doi.org/10.3390/photonics6020055. Article № 55.
[30] Anashkina EA, Sorokin AA, Marisova MP, Andrianov AV. Development and numerical simulation of tellurite glass microresonators for optical frequency comb generation. J Non-Cryst Solids 2019;522:119567https://doi.org/10.1016/j.jnoncrysol.2019.119567.
[31] Oraevsky AN. Whispering-gallery waves. Quantum Electr 2002;32:377–400. https://doi.org/10.1070/QE2002v032n05ABEH002205.
[32] Payne S, Chase L, Smith L, Kway W, Krupke W. Infrared cross-section measurements for crystals doped with Er^{3+}, Tm^{3+} and Ho^{3+}. IEEE J Quantum Electron 1992;28:2619–30. https://doi.org/10.1109/3.161321.
[33] McCumber D. Theory of phonon-terminated optical masers. Phy Rev 1964;136:A299–306. https://doi.org/10.1103/PhysRev. 134.A299.
[34] Braginsky VB, Gorodetsky ML, Ilchenko VS. Quality-factor and nonlinear properties of optical whispering-gallery modes. Phys Lett A 1989;137:393. https://doi.org/10.1016/0375-9601(89)90912-2.
[35] Gomes L, Lousteau J, Milanese D, Scarpignato GC, Jackson SD. Energy transfer and energy level decay processes in Tm^{3+}-doped tellurite glass. J Appl Phys 2012;111:063105https://doi.org/10.1063/1.3694747.
[36] Anashkina EA, Kim AV. Numerical simulation of ultrashort mid-IR pulse amplification in praseodymium-doped chalcogenide fibers. J Light Technol 2017;35:5397–403. https://doi.org/10.1109/JLT.2017.2775864.
[37] Min B, Kippenberg TJ, Yang L, Vahala KJ, Kalkman J, Polman A. Erbium-implanted high-Q silica toroidal microcavity laser on a silicon chip. Phys Rev A 2004;70:033803https://doi.org/10.1103/PhysRevA.70.033803.
[38] Mescia L, Bia P, De Sario M, Di Tommaso A, Prudenzano F. Design of mid-infrared amplifiers based on fiber taper coupling to erbium-doped microspherical resonator. Opt Express 2012;20:7616–29. https://doi.org/10.1364/OE.20.007616.
[39] Gorodetsky ML, Savchenkov AA, Ilchenko VS. Ultimate Q of optical microsphere resonators. Opt Lett 1996;21:453–5. https://doi.org/10.1364/OL.21.000453.
[40] Little BE, Laine JP, Haus HA. Analytic theory of coupling from tapered fibers and half-blocks into microsphere resonators. J Lightwave Technol 1999;17:704–15. https://doi.org/10.1109/50.754802.